Acta Mech 225, 2385–2407 (2014)
DOI 10.1007/s00707-014-1130-4

Brian P. Lawney · Stefan Luding

Frequency filtering in disordered granular chains

Received: 27 February 2013 / Revised: 11 July 2013 / Published online: 28 June 2014

Abstract The study of disorder-induced frequency filtering is presented for one-dimensional systems composed of random, pre-stressed masses interacting through both linear and nonlinear (Hertzian) repulsive forces. An ensemble of such systems is driven at a specified frequency, and the spectral content of the propagated disturbance is examined as a function of distance from the source. It is shown that the transmitted signal contains only low-frequency components, and the attenuation is dependent on the magnitude of disorder, the input frequency, and the contact model. It is found that increased disorder leads to a narrower bandwidth of transmitted frequencies at a given distance from the source and that lower input frequencies exhibit less sensitivity to the arrangement of the masses. Comparison of the nonlinear and linear contact models reveals qualitatively similar filtering behavior; however, it is observed that the nonlinear chain produces transmission spectrums with a greater density at the lowest frequencies. In addition, it is shown that random masses sampled from normal, uniform, and binary distributions produce quantitatively indistinguishable filtering behavior, suggesting that knowledge of only the distribution's first two moments is sufficient to characterize the bulk signal transmission behavior. Finally, we examine the wave number evolution of random chains constrained to move between fixed end-particles and present a transfer matrix theory in wave number space, and an argument for the observed filtering based on the spatial localization of the higher-frequency normal modes.

1 Introduction

One-dimensional analogs of electronic, magnetic, and mechanical systems are often employed for their use as simple models which have the potential to reveal the physics of more general, higher-dimensional systems [25]. As a subset of these problems, chains of non-cohesive particles have received significant attention in the literature. Linear arrangements of harmonic oscillators are common in the introduction to lattice vibrations in solid state physics [12,50]. These treatments are typically limited to infinitely repeatable unit cells containing one or two particles/atoms for which dispersion equations relating the oscillation frequency and wavelength are analytically accessible. It is from these periodic, linear systems that more recent studies on inhomogeneous, disordered, and nonlinear chains originate.

The introduction of nonlinear (e.g., Hertzian) particle interactions resembles most experiments with granular chains of pre-stressed elastic spheres and leads to novel behavior such as soliton-like nonlinear waves [2,17,28–30,37,44]. Sen et al. [43] provide a detailed account of prior studies concerning solitary waves in granular chains. Note that many studies focus on uncompressed chains where particles are barely in contact. Additionally, there is significant attention placed on the behavior of "designed" and ordered nonlinear

Presented at the 8th European Solid Mechanics Conference in the Graz University of Technology, Austria, July 9–13, 2012.

B. P. Lawney · S. Luding (✉)
Multiscale Mechanics (MSM), MESA+, Faculty of Engineering Technology (CTW),
PO Box 217, 7500 AE Enschede, The Netherlands
E-mail: s.luding@utwente.nl

chains, often motivated by energy modification and shock-protection applications. Studies have employed smoothly varying mass distributions [40], "decoration" (e.g., deliberate insertion of different sized masses) [10,13,14,27] tapering [5,32,47,49] and controlled variation of the particle material [3,15]. Combinations of both tapering and decoration have also been employed [6,13]. The interest in non-linear, realistic wave-propagation phenomena is documented by the most recent publications on contact dissipation mechanisms in one-dimensional [31,36,38] and higher dimensional idealized granular systems [7,24,31].

The inclusion of disorder through mass, size, or interaction (stiffness) variation (and combinations thereof) is a natural extension reflecting the disordered, inhomogeneous state of many realistic discrete systems. One-dimensional systems provide a simple framework to study the basic effects of disorder without consideration for the geometric complexity of higher dimensions, thus excluding the scattering of signals to other directions. Analysis of the spectrum and density of eigenstates was the subject of many early studies in disordered one-dimensional systems [4,8,33,42]. In the context of quantum mechanical particles, Anderson [1] noted the localization of the wavefunctions in the presence of sufficiently strong random potentials. This "Anderson localization" has been confirmed in disordered mechanical systems of vibrating masses [23,41].

As with tapered and decorated chain arrangements, recent studies of random granular arrays show an interest in the use of these systems to dissipate or enhance energy propagation. Nesterenko [37] examined the downstream speed and energy of particles in nonlinear random chains following an initial excitation applied to one end of the system. It was reasoned that complex nonlinear interactions between the chain members make the system behavior difficult to predict in general. Manciu et al. [30] report a spatially exponential decrease in the incident kinetic energy for various amounts of mass disorder, with increasing disorder leading to a faster energy loss. Fraternali et al. [9] employed an evolutionary algorithm which generated random "protecting" chains whose effectiveness was evaluated by the force transmitted at the end of the system. It was noted that temporally short and high amplitude pulses were transformed to low amplitude, longer wavelength (temporally longer) signals at the downstream receiver. Ponson et al. [39] employ a nonlinear chain of two-particle unit cells which are randomly oriented, as in a spin system, and studies the effect of their disorder parameter on the spatial decay of the force transmitted by such systems. Harbola et al. [14] decorate monodisperse chains with randomly sized small masses and investigate the propagation time and decay of the pulse velocity as a function of system penetration.

Studies concerning the frequency-filtering effects of disorder have received less attention than energy or force attenuation. Jia et al. [16] report experimental studies on ultrasound propagation through three-dimensional packings of glass beads. The time and frequency analysis of the transmitted signal reveal the appearance of an initial pulse close to the source that contains relatively low frequencies with respect to the input spectrum. The initial pulse is followed by an irregular signal, i.e., the "coda," that contains the higher frequencies, consistent with the lower phase velocity of higher-frequency components. The spectrum of this irregular signal seems to indicate more attenuation of the high-frequency components. Judge et al. [18] numerically examine the spectra of disordered micromechanical oscillators, focusing on frequency filtering within the passband of ordered arrays. They note the significant change in the transmitted spectrum with increasing disorder and the propagation of frequencies associated with the natural frequency of the individual oscillators. The low-pass filtering seen does not seem to be observed, likely due to the short length of the arrays considered (5 oscillators). Mouraille and Luding [34,35] numerically studied the high-frequency filtering present in three-dimensional packings perturbed from their perfect crystalline geometry by a small random variation in the particle sizes. Following a delta-like pulse of the boundary, only the low-frequency components of the excitation are observed to propagate a significant distance. The polydispersity introduced is quite small with respect to the particle length scale (0.2 % variation), but as this change is comparable to the contact length scale remarkable differences in the propagation characteristics of the medium are observed.

It is worth noting that nonlinear particle interactions permit frequency mixing behavior. Given excitations at frequencies ω_1 and ω_2, a component at the difference-frequency $|\omega_2 - \omega_1|$ is generated, among others. For sufficiently close magnitudes, this is a low-frequency component. In realistic materials, the high frequencies are attenuated and only the difference-frequency is seen to propagate a significant distance. Tournat et al. [48] observe the propagation of these low-frequency signals in nonlinear chains, terming itself demodulation. However, such behavior is due to nonlinear interaction and is not a mass disorder-induced effect. Frequency mixing due to disorder was also noted by Mouraille [34].

In this paper, we study the effect of disorder and nonlinearity on the transmission of signals in one-dimensional systems. We consider initially static, pre-stressed configurations with given disorder magnitude that are subjected to a harmonic perturbation of the boundary. Prescribing a perturbation frequency, we average over many configurations of the chain to observe ensemble-averaged behavior. In Sect. 2, we derive the

equations of motion that govern the idealized system. In particular, the linear and Hertzian force models are given in Sects. 2.1.2 and 2.1.3, respectively. Using these relations, we examine the effects of disorder on the high-frequency-filtering behavior in Sect. 3 and summarize and conclude in Sect. 4.

2 Modeling

In this section, the equations of motion are derived employing a general nonlinear force–displacement relation. Two specific cases follow, corresponding to the harmonic (linear) and Hertzian models.

2.1 Compressed chain

In this study, we consider one-dimensional arrays of $(N+2)$ random mass particles which interact with only their immediate neighbors in a purely repulsive manner. In addition, we consider chains that are pre-compressed such that there is some initial strain associated with the equilibrium configuration. The absolute position, radius, and mass of a general particle j are given by $\tilde{x}^{(j)}$, $\tilde{r}^{(j)}$, and $\tilde{m}^{(j)}$, respectively. Anticipating an appropriate scaling of the problem, we employ the tilde symbols to denote dimensional quantities. The interaction force between neighboring particles i and j is modeled as

$$\left|\tilde{F}_{(i,j)}\right| = \tilde{\kappa}_{(i,j)}\tilde{\delta}_{(i,j)}^{1+\beta}, \quad \tilde{\delta}_{(i,j)} \geq 0, \tag{1}$$

where $\tilde{\kappa}_{(i,j)}$ is a "stiffness" that changes with the value of β and depends, in general, on the properties of the contacting bodies. The particle overlap is given as $\tilde{\delta}_{(i,j)} = \tilde{r}^{(i)} + \tilde{r}^{(j)} - |\tilde{x}^{(j)} - \tilde{x}^{(i)}|$ such that it is strictly non-negative for contacts. The Hertz and linear models are given by $\beta = 1/2$ and $\beta = 0$, respectively [22,26,37]. Choosing a length scale $\tilde{\ell}$ (to be determined later), we scale the particle overlap:

$$\left|\tilde{F}_{(i,j)}\right| = \tilde{\kappa}_{(i,j)}\tilde{\ell}^{1+\beta}\delta_{(i,j)}^{1+\beta}, \tag{2}$$

where $\delta_{(i,j)} \equiv \tilde{\delta}_{(i,j)}/\tilde{\ell}$. Compressing the chain by an applied force $\tilde{P}$, the dimensionless initial particle overlap at the contact between i and j is

$$\Delta_{(i,j)} = \left(\frac{\tilde{P}}{\tilde{\kappa}_{(i,j)}\tilde{\ell}^{1+\beta}}\right)^{1/(1+\beta)}. \tag{3}$$

Associated with the length scale $\tilde{\ell}$, we have a characteristic mass $\tilde{m}_o$, which we take as the mean particle mass of the system. Dimensional analysis yields a timescale

$$\tilde{t}_c = \frac{1}{\tilde{\ell}^{\beta/2}}\sqrt{\frac{\tilde{m}_o}{\tilde{\kappa}_o}}, \tag{4}$$

where $\tilde{\kappa}_o$ functions as the characteristic stiffness of the system. This will be defined with respect to the contact of two identical particles of the mean mass, $\tilde{m}_o$. In the nonlinear cases, $(\beta \neq 0)$ $\tilde{\ell}$ factors into this timescale. We may write an equation of motion for the general particle i $(i = 1, \ldots, N)$ as:

$$\tilde{m}^{(i)}\frac{d^2\tilde{x}^{(i)}}{d\tilde{t}^2} = \tilde{\kappa}_{(i-1,i)}\tilde{\ell}^{1+\beta}\delta_{(i-1,i)}^{1+\beta} - \tilde{\kappa}_{(i+1,i)}\tilde{\ell}^{1+\beta}\delta_{(i+1,i)}^{1+\beta}. \tag{5}$$

We denote the displacement of particle i from its equilibrium position $\tilde{x}_o^{(i)}$ as $\tilde{u}^{(i)} = \tilde{\ell}u^{(i)} = \tilde{x}^{(i)} - \tilde{x}_o^{(i)}$. Thus, for a contact between i and j (with $j > i$), the scaled overlap is $\delta_{(i,j)} = \Delta_{(i,j)} - (u^{(j)} - u^{(i)})$. With dimensionless mass $b^{(i)} \equiv \tilde{m}^{(i)}/\tilde{m}_o$ and time $\tau \equiv \tilde{t}/\tilde{t}_c$, we write

$$\begin{aligned} b^{(i)}\frac{d^2u^{(i)}}{d\tau^2} &= \kappa_{(i-1,i)}\left[\Delta_{(i-1,i)} - u^{(i)} + u^{(i-1)}\right]^{1+\beta} \\ &\quad - \kappa_{(i+1,i)}\left[\Delta_{(i+1,i)} + u^{(i)} - u^{(i+1)}\right]^{1+\beta}, \end{aligned} \tag{6}$$

where the stiffness ratio $\kappa_{(i,j)} = \tilde{\kappa}_{(i,j)}/\tilde{\kappa}_o$ has been defined implicitly.

For the particles 1 and N, we write equations of motion associated with the imposed boundary conditions. We harmonically displace particle 0 at angular frequency $\omega_o = \tilde{\omega}_o \tilde{t}_c$ and fix particle $(N+1)$:

$$u^{(0)}(\tau) = \epsilon \sin \omega_o \tau, \tag{7}$$

$$u^{(N+1)}(\tau) = 0, \tag{8}$$

where $\epsilon = \tilde{\epsilon}/\tilde{\ell}$ is the scaled oscillation amplitude. Thus, the coupled system of differential equations governing the modeled system is given by (6) with substitution of (7) and (8) for $i = 1$ and $i = N$, respectively.

There are various choices available for the length scale $\tilde{\ell}$. One could use the particle size or the driving amplitude. However, we choose the length scale to be related to the overlap of a characteristic contact in static equilibrium. As in defining the characteristic stiffness, we consider the contact of two identical particles of the mean mass. Under the applied compressive force, the initial overlap between such particles provides us with $\tilde{\ell} = \tilde{\Delta}_o$ ($\Delta_o = 1$). In a typical simulation, the scaled driver amplitude $\epsilon \ll \Delta_o$ is chosen so as not to cause an opening of contacts. However, we explore driver amplitudes that approach the contact length scale under the restriction that particles remain in contact at all times. Note that ϵ incorporates the pre-compression of the system through (3):

$$\epsilon = \frac{\tilde{\epsilon}}{\tilde{\Delta}_o} = \tilde{\epsilon} \left(\frac{\tilde{\kappa}_o}{\tilde{P}} \right)^{2/3}. \tag{9}$$

Since $\tilde{\kappa}_o$ is set by the size of the particles (see Appendix 2), small values of ϵ represent systems with small driving and/or a large pre-stress through $\tilde{P}$.

2.1.1 Linearized equations of motion

Here, we linearize the general force–displacement relation about the equilibrium configuration. The non-dimensional phrasing of (1) is given by

$$F_{(i,j)}(\delta_{(i,j)}) = \kappa_{(i,j)} \delta_{(i,j)}^{1+\beta}. \tag{10}$$

Expanding about the equilibrium position $\Delta_{(i,j)}$, we obtain

$$\begin{aligned} F_{(i,j)}(\delta_{(i,j)}) = {} & \kappa_{(i,j)} \Delta_{(i,j)}^{1+\beta} + \kappa_{(i,j)}(1+\beta)\Delta_{(i,j)}^{\beta}(\delta_{(i,j)} - \Delta_{(i,j)}) \\ & + \frac{\kappa_{(i,j)}\beta(1+\beta)\Delta_{(i,j)}^{\beta-1}}{2}(\delta_{(i,j)} - \Delta_{(i,j)})^2 + \cdots \end{aligned} \tag{11}$$

Assuming small displacements from equilibrium, we retain only the constant and linear terms. With $\delta_{(i,j)} = \Delta_{(i,j)} - (u^{(j)} - u^{(i)})$ for particle indices such that $j > i$, we obtain

$$F_{(i,j)}(\delta_{(i,j)}) = \kappa_{(i,j)} \Delta_{(i,j)}^{1+\beta} - \kappa_{(i,j)}(1+\beta)\Delta_{(i,j)}^{\beta} \left(u^{(j)} - u^{(i)} \right), \tag{12}$$

which is the linearized force of particle i on particle j for $j > i$. The equation of motion for a general particle i is then

$$\begin{aligned} b^{(i)} \frac{d^2 u^{(i)}}{d\tau^2} = {} & \kappa_{(i-1,i)} \Delta_{(i-1,i)}^{\beta} \left[\Delta_{(i-1,i)} - (1+\beta) \left(u^{(i)} - u^{(i-1)} \right) \right] \\ & - \kappa_{(i+1,i)} \Delta_{(i+1,i)}^{\beta} \left[\Delta_{(i+1,i)} - (1+\beta) \left(u^{(i+1)} - u^{(i)} \right) \right]. \end{aligned} \tag{13}$$

2.1.2 Linear coupling: $\beta = 0$

In the case of $\beta = 0$, we recover the harmonic chain with linear springs between the mass elements. The linear contact model is appropriate for chains with sufficiently high confining force; Sinkovits et al. [46] show

that the frequency spectrum of oscillations approaches that of a harmonic chain with increasing compressive force. As expected, the general equations of motion (6) and the linear expansion (13) match exactly. We may compactly express the N linear equations in the matrix form

$$\mathbf{M}\frac{\mathrm{d}^2\mathbf{u}}{\mathrm{d}\tau^2} = \mathbf{K}\mathbf{u} + \mathbf{f}, \tag{14}$$

where $\mathbf{M}$ is a diagonal matrix with the random mass ratios $b^{(1)}$ through $b^{(N)}$ on the diagonal, and $\mathbf{K}$ is a symmetric, tri-diagonal matrix. The sub- and super-diagonal elements are given by $\mathbf{K}(i, i-1) = \kappa_{(i-1,i)}$ and $\mathbf{K}(i, i+1) = \kappa_{(i+1,i)}$, respectively. The diagonal entries are $\mathbf{K}(i, i) = -(\kappa_{(i-1,i)} + \kappa_{(i+1,i)})$. Since the stiffnesses depend on the contacting particles, these values are random in general. The forcing vector $\mathbf{f}$ has only one nonzero entry, which is $f_1(\tau) = \epsilon \sin \omega_o \tau$ in the first position. Other entries cancel by the equilibrium condition $\kappa_{(i-1,i)}\Delta_{(i-1,i)} = \kappa_{(i+1,i)}\Delta_{(i+1,i)}$.

Since we look to examine the effect of mass disorder alone, we take all coupling stiffnesses to be independent of the contact ($\kappa_{(i,j)} = 1$). Accordingly, all initial overlaps are equal with $\Delta_{(i,j)} = 1$. With this assumption, the stiffness matrix simplifies, with $\mathbf{K}$ now having entries of -2 on the diagonal and entries of $+1$ on the sub- and super-diagonal.

We examine the solutions of the linear system (14) in Sect. 2.2.

2.1.3 Nonlinear Hertzian coupling: $\beta = 1/2$

With $\beta = 1/2$, we obtain the Hertz contact model and the equations of motion are given by (6), (7), and (8). The interparticle forces are dependent on the size and material properties of the constituent particles (see Appendix 2). We find that the scaled stiffness $\kappa_{(i,j)}$ and initial overlap $\Delta_{(i,j)}$ are given by

$$\kappa_{(i,j)} = \sqrt{\frac{2}{b^{(i)1/3} + b^{(j)1/3}}}\left(b^{(i)}b^{(j)}\right)^{1/6}, \tag{15}$$

and

$$\Delta_{(i,j)} = \kappa_{(i,j)}^{-2/3}. \tag{16}$$

As in the linearized version of the Hertz chain of given by (14), the nonlinear chain of polydisperse spheres is, in general, disordered in both mass and coupling stiffness.

2.1.4 Creation of mass-disordered, monodisperse chains

A general polydisperse chain of masses will be disordered in mass and interparticle contact stiffness. If we wish to remove the effects of this "contact disorder" (as present in the Hertzian model), one may consider the modification of particles to create a monodisperse (size) chain of varied mass. In this manner, we isolate the effect of mass disorder. Numerically incorporating such a construction is trivial; the equations of motion are given by (6), (7), and (8), and we assign $\kappa_{(i,j)} = 1$ and $\Delta_{(i,j)} = 1$ for all contacts (i, j). In an experimental realization, one may imagine creating such a monodisperse, mass-disordered chain by the removal of material from the particle centers or the inclusion of denser cores. Since the Hertz model is based on deformations local to the contacting surfaces, this change in mass should have a negligible effect on the contact stiffnesses provided the modification is sufficiently far from the surface.

2.2 Linear model: analysis

With the goal of solving for the general motion of the linear chain under the imposed boundary conditions, we look to state (14) in its eigenvector basis. This transformation decouples the equations of motion into N independent relations, facilitating the process of finding a general solution. Upon determination of the solution in the eigensystem, a simple linear transformation yields the motion of the particles.

Thus, we first seek to determine the eigenvectors and eigenfrequencies associated with (14). We set $\mathbf{f} = \mathbf{0}$ and assume that for each normal mode all masses oscillate with a particular frequency ω. Defining $\mathbf{A} \equiv -\mathbf{M}^{-1}\mathbf{K}$ (not symmetric, in general), we arrive at the familiar eigenvalue problem:

$$\mathbf{A}\mathbf{u} = \omega^2\mathbf{u}. \tag{17}$$

This may be solved numerically to determine the set of N orthonormal eigenmodes $\{\mathbf{s}_{(j)}\}$ and eigenfrequencies $\{\omega_{(j)}\}$. We normalize the eigenvectors to have the following orthonormality conditions (see Appendix 1):

$$\mathbf{s}_{(i)}^{\mathrm{T}}\mathbf{M}\mathbf{s}_{(j)} = \delta_{ij}, \tag{18}$$

where δ_{ij} is the usual Kronecker delta symbol.

We sort the eigenvectors by increasing order of their associated eigenvalues (frequencies) and assemble the $(N \times N)$ matrix $\mathbf{S}$ such that the jth column is eigenvector $\mathbf{s}_{(j)}$. Using $\mathbf{S}^{-1}$ as the transformation matrix between the particle displacements $\mathbf{u}$ and the eigenmode amplitudes $\mathbf{z}$, we have $\mathbf{z} = \mathbf{S}^{-1}\mathbf{u}$. We also note the similarity transform $\mathbf{S}^{-1}\mathbf{A}\mathbf{S} = \mathbf{D}$, where $\mathbf{D}$ is a diagonal matrix with the (increasing) eigenvalues along the diagonal.

With the use of $\mathbf{S}$, we transform the general equation of motion (14) and obtain the decoupled form

$$\frac{\mathrm{d}^2\mathbf{z}}{\mathrm{d}\tau^2} = -\mathbf{D}\mathbf{z} + \mathbf{h}, \tag{19}$$

where $\mathbf{h} = \mathbf{S}^{-1}\mathbf{M}^{-1}\mathbf{f}$. In our specific case of harmonic driving, the transformed forcing vector $\mathbf{h}$ may be rephrased as follows. Since $\mathbf{f} = \epsilon \sin\omega_o\tau\mathbf{e}_1$ ($\mathbf{e}_1 = [1\ 0\ \ldots\ 0]^{\mathrm{T}}$), we have

$$\mathbf{h} = \mathbf{S}^{-1}\mathbf{M}^{-1}\epsilon \sin\omega_o\tau\mathbf{e}_1 = \epsilon \sin\omega_o\tau\mathbf{y}, \tag{20}$$

where $b^{(1)}\mathbf{y} \equiv \mathbf{S}^{-1}\mathbf{e}_1$ is the first column of $\mathbf{S}^{-1}$. Exploiting the orthogonality given in (18), we left-multiply $\mathbf{y}$ by $\mathbf{S}^{\mathrm{T}}\mathbf{M}\mathbf{S} = \mathbf{I}$ and find $\mathbf{y} = \mathbf{S}^{\mathrm{T}}\mathbf{e}_1$. Thus, $\mathbf{y}$ is the first *row* of $\mathbf{S}$.

The general solution to (19) is then,

$$\mathbf{z} = \mathbf{C}^{(1)}\mathbf{a}^{(1)} + \mathbf{C}^{(2)}\mathbf{a}^{(2)} + \epsilon \sin\omega_o\tau\mathbf{c}, \tag{21}$$

where $\mathbf{C}^{(1)}$ and $\mathbf{C}^{(2)}$ are diagonal matrices with (j, j) entries $\sin\omega_j\tau$ and $\cos\omega_j\tau$, respectively. The vectors $\mathbf{a}^{(1)}$ and $\mathbf{a}^{(2)}$ are determined from the initial conditions of the displacement $\mathbf{u}(0) = \mathbf{u}_o$ and velocity $\dot{\mathbf{u}}(0) = \mathbf{v}_o$. Vector $\mathbf{c}$ has j^{th} entry $S_{1j}/(\omega_j^2 - \omega_o^2)$. Employing the initial conditions, we obtain

$$\mathbf{a}^{(1)} = \mathbf{W}^{-1}\mathbf{S}^{-1}\mathbf{v}_o - \epsilon\,\omega_o\mathbf{W}^{-1}\mathbf{c}, \tag{22}$$

$$\mathbf{a}^{(2)} = \mathbf{S}^{-1}\mathbf{u}_o. \tag{23}$$

Here, $\mathbf{W}^{-1}$ is a diagonal matrix with $1/\omega_{(j)}$ as the (j, j) entry. If we specify initial conditions $\mathbf{u}_o = \mathbf{v}_o = \mathbf{0}$ and transform back to displacement space via $\mathbf{S}$, we obtain the displacement history of particle p,

$$u^{(p)}(\tau) = \epsilon \sum_{j=1}^{N} \frac{S_{pj}S_{1j}}{\left(\omega_{(j)}^2 - \omega_o^2\right)}\left(\sin\omega_o\tau - \frac{\omega_o}{\omega_{(j)}}\sin\omega_{(j)}\tau\right). \tag{24}$$

For a given chain arrangement, we may calculate the displacement history from (24), and this way investigate the frequency spectrum at a particular location in the chain. Discussion of the terms in (24) is deferred to Sect. 3.3.

We finally note that in the case of an undriven ($\epsilon = 0$) monodisperse linear chain, we obtain the dispersion relation [50]

$$\omega(k) = 2\sin(k^*/2), \tag{25}$$

where $k^* = d_0k = 2\pi d_0/\lambda$ is the dimensionless wave number (purely real) scaled by the particle diameter. This sets the cutoff frequency for propagative waves at $\omega \le \omega_{\max} = 2$. At $\omega_{\max} = 2.0$, we have the minimum scaled wavelength $\lambda^*_{\min} = \lambda/d_0 = 2$. That is, signal frequency components in the passband of $0 < \omega \le 2$ propagate without attenuation. Frequencies above the cutoff are termed evanescent waves as the wave number has an imaginary component which causes the signal to exponentially decay with distance. Since our random chains contain masses distributed about the monodisperse system of $b^{(i)} = 1$, we will consider driving frequencies ω_o on the order of $\omega = 2$, in the range $[0.1\omega_{\max}, 1.6\omega_{\max}]$.

3 Results and discussion

In this section, we present results on the high-frequency-filtering effects of random chains.

Section 3.1 discusses the construction of the random systems for several mass distributions. We also introduce our definition of the disorder parameter.

Section 3.2.1 contains results for the chain with linear contact forces, with masses chosen from a normal mass distribution and uniform contact stiffness, examining the effects of disorder and driving frequency. A comparison of mass distributions is shown in 3.2.2, and Sect. 3.2.3 investigates the role of coupling (contact stiffness) disorder in harmonic chains.

Sections 3.3.1 and 3.3.2 focus on the effect of disorder on the density of states and localization, while Sect. 3.3.3 features the wave number spectra evolution with time for an inserted standing wave.

Results related to the nonlinear chain are presented in Sect. 3.4. Similar to the linear chain, we perform a parameter study in Sect. 3.4.1 and examine the effect of disorder and driving frequency. The driving amplitude is also considered. We follow this in Sect. 3.4.2 with results for the nonlinear chain featuring uniform contact interactions, which isolates the effect of mass disorder.

3.1 Chain generation

We introduce mass disorder to the chains by randomly sampling from a specified probability distribution. A seeded random number generator with the appropriate statistical properties is created to generate the masses. In this study, we consider normal $f^{(n)}(b)$, uniform $f^{(u)}(b)$, and binary discrete $f^{(d)}(b)$ distributions, where b is the scaled mass.

For the normal distribution of masses, we prescribe the mean $\bar{b} = 1$ and standard deviation ξ, which will be used to quantify the disorder of the system. When sampling masses to create the normally distributed random chains, we enforce a lower cutoff such that $b > 0$. No such cutoff is implemented for the largest masses. In Fig. 1, we plot the ensemble-averaged $\langle b_{\min} \rangle$ and $\langle b_{\max} \rangle$. For each figure, we average over a set of 10^5 chains sampled from a normal distribution, with each chain containing 2,000 particles. We note that the restriction of $b > 0$ causes the ensemble-averaged minimum mass values to be bounded as we increase the width of the distribution (disorder) ξ. Values of the largest ensemble-averaged masses increase linearly with ξ, as expected.

For comparison between the three distributions, we match the first two moments of the theoretical probability density functions. By employing three different mass distributions that have the same moments, we may compare the filtering behavior of these systems and investigate the role of the mass distribution. In general, the n^{th} moment of a given distribution $f^{(q)}(b)$ is defined as

$$M_n^{(q)} = \int_{-\infty}^{\infty} b^n f^{(q)}(b)\, \mathrm{d}b, \tag{26}$$

where q is used to identify the specific distribution type. Since only positive masses are permitted, the lower limit of integration may be changed to zero. With $M_1^{(n)} = 1$ and $M_2^{(n)} = 1+\xi^2$, we calculate the corresponding limits of the uniform distribution to be $1 \pm \sqrt{3}\xi$. For the binary distribution, the masses are placed at $1 \pm \xi$.

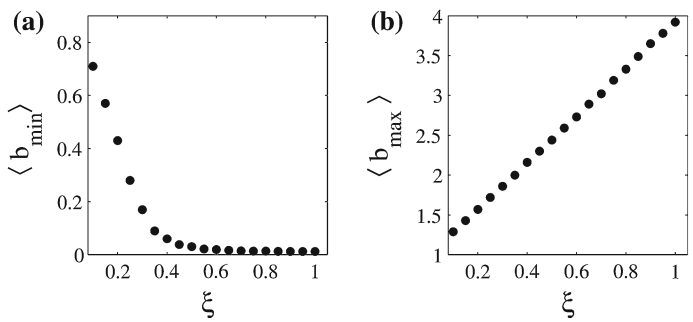

Fig. 1 Ensemble-averaged minimum and maximum masses. The masses are sampled from a normal distribution with mean $\bar{b} = 1$ and standard deviation ξ. Each chain contains 2,000 particles and the ensemble has 10^5 chains

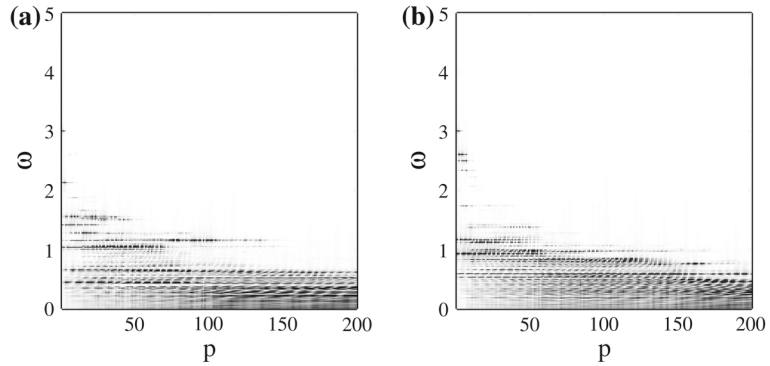

Fig. 2 Frequency propagation spectrum as a function of distance (in mean particle diameters) from the source for two instances of a single realization of a normally distributed disordered chain with uniform linear coupling. $\xi = 0.5$, $\omega_o = 3$, $\mathrm{d}\tau = 0.0667$, $\tau_{\max} = 546.41$, $N = 500$, $M = 200$

For the binary distribution to be symmetric about the mean, large and small masses are selected with equal probability; the probability of there being j or greater successive equal masses is $\approx 2^{-j}$. Long monodisperse sections which might significantly affect the transmission properties of the chain are thus unlikely.

When comparing the various mass distributions, we restrict $\xi \leq 0.5$, neglecting $\approx 2.3\,\%$ of the normal distribution where $b < 0$. In the context of our parameter study employing only normally distributed masses, we consider $\xi \leq 1$.

3.2 Linear chain filtering

Given an array of $(N + 2)$ random masses (where the end-particles have prescribed motion), we numerically solve the eigenvalue problem as described in Sect. 2.2, yielding the $(N \times N)$ eigenvector matrix $\mathbf{S}$ and the N eigenfrequencies $\{\omega_{(j)}\}$ $(j = 1, \ldots, N)$. With Eq. (24), we calculate the displacement history $u^{(p)}(\tau_n)$ of particle p at discrete time steps $\tau_n = n\mathrm{d}\tau$ on the interval $\tau = [0, \tau_{\max}]$. The time window is sufficiently large, and the scaled time step $\mathrm{d}\tau$ is chosen to be small enough to permit sampling at the frequencies of interest. We then perform a discrete Fourier transform to obtain the spectrum of this signal. In particular, we examine the absolute value of the Fourier components, $U^{(p)}(\omega)$. This calculation is performed for particles $p = 1, \ldots, M$. The length of the chain $(N+2)$, the sampling region length M, and the time window $\tau_{\max}$ are chosen such that the disturbance signal has not reached the end-particle $p = N + 1$ and thus is not reflected back, preventing interference from reflected waves. Additionally, the parameters are chosen such that the high frequencies (with corresponding lower phase velocity) have been given sufficient time to propagate through the sampling region; if the time duration were too short, then the "filtering" could, in fact, only be a measurement artifact.

The spectra of oscillations for the sampled particles may be compactly visualized by the use of a three-dimensional plot projected into a two-dimensional plane. Here, we plot in the (p, ω) plane and represent the values of the absolute Fourier components $|U^{(p)}(\omega)|$ in gray scale. At each location p, the $|U^{(p)}(\omega)|$ array of values is normalized to unity (which allows us to compare their relative contribution). In our convention, darker shades correspond to larger values with the scaling set such that black corresponds to a Fourier component $\geq$0.2. This is applied for all of the following figures. For two particular chain arrangements, we obtain Fig. 2. We will later show averages over 200 different realizations.

In both of Fig. 2a, b, we note a rapid decrease in the input frequency within several particle diameters from the driver. Following this, we observe the persistence of several lower frequencies $(\omega < \omega_o)$ which are dependent on the particular chain arrangement. However, by $p = 200$, we note that the frequency content of the two arrangements is more comparable and frequencies $\omega \gtrapprox 0.5$ have absolute Fourier components that are relatively small with respect to $\omega \lessapprox 0.5$. This range of propagated frequencies is dependent on the disorder parameter, as investigated in Sect. 3.2.1.

Examining the evolution of a particular frequency component ω^* as it propagates down the chain, we note the dark and light oscillations ("stitching") apparent for certain frequencies in both plots of Fig. 2. For lower frequencies, the wavelengths of these features match closely with those obtained from the dispersion relation (25) for the perfect chain, as shown in Fig. 3. Here, for a single chain realization, we compare the features of the dispersion relation to the spatial filtering behavior. To construct this figure, we perform a discrete double

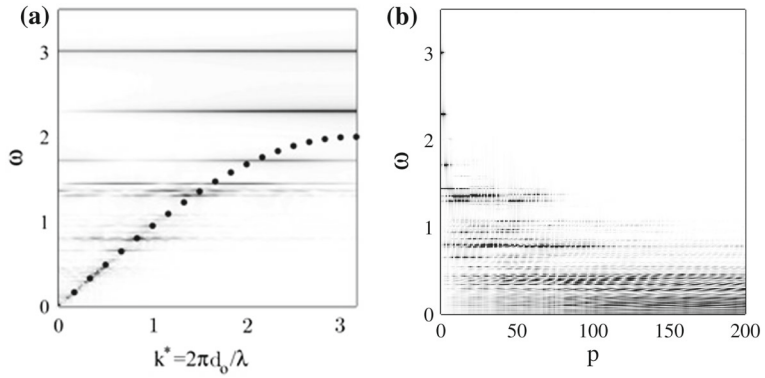

Fig. 3 Dispersion relation (**a**) obtained from the simulation displayed in (**b**). The *black circles* are obtained from the perfect chain ($\xi = 0$) dispersion relation (25) at 20 equidistant k^* values. *Darker shades* correspond to greater magnitude Fourier components. The horizontal stripes in **a** for $w > 2$ are due to the input signal at the first few particles, $p < 5$, and vanish if the space-Fourier-transform is carried out using only $p \geq 5$

Fourier transform of the $u^{(p)}(\tau)$ signal. With this plot, we may examine the wavelength λ of the stitching as ω^* is varied. Note the close agreement between the analytical result (black circles) and the data in the low-frequency/long-wavelength limit ($\omega < 0.5$). As the frequency increases, there is significant deviation of the disordered system from the monodisperse chain. The dark horizontal lines change with the particular chain arrangement and correspond to strong, but spatially short excitations, indicating localization of the oscillations at frequency ω^*.

The light areas of the stitching thus correspond to nodes of the wave, where the magnitude of oscillations at a particular frequency ω^* are insignificant. Based upon the chain arrangement, this behavior is more visually apparent at certain frequencies, but Fig. 3 confirms that there is a "selected" wavelength associated with the oscillations for intermediate to low frequencies. We note that the stitching is a consequence of the wave component interactions since it is not present in our simulations with perfect chains; in such cases, a monochromatic horizontal line is observed to propagate without change (if in the passband, $\omega \leq 2$). Simulations of perfect chains produce dispersion plots that exactly match the black circles plotted in Fig. 3.

3.2.1 Frequency filtering of the monodisperse linear chain: normally distributed masses

Here, we employ a normal distribution of masses and perform a parameter study on the effects of disorder magnitude ξ and source frequency ω_o. For each set of data, we generate an ensemble of 200 random chains (with different random masses; however, for the equal-mass chain, this has no effect due to lack of random disorder, i.e., $\xi = 0$). Each chain contains $N = 500$ particles, and we examine the displacement signal for particles 1 through $M = 200$. Selection of the chain length N and the value of M is based on examining the results of longer systems; for relatively high disorder ($\xi = 0.5$), we note minimal change in the spectrum of transmitted frequencies beyond approximately 200 particles from the excitation source.

By requiring that the signal does not reach the fixed end-particle $p = (N + 1)$, a sampling time interval $\tau = [0, \tau_{\max}]$ is approximately determined from the analysis of several chain arrangements ("microstates"). If the fixed end is indeed reached in a particular microstate, the reflected signal certainly does not have sufficient time to propagate backwards to the sampling region, $p < M$.

With $\tau_{\max}$ set, we divide the time span into q steps such that $\mathrm{d}\tau = \tau_{\max}/q$ is small enough to detect the relevant large frequencies in a given signal. As stated in Sect. 2.2, a monodisperse linear chain will propagate normalized frequencies $\omega \leq 2$, and we drive the disordered chains at frequencies of this order. We select $q = 8{,}192$ time steps which yields $\mathrm{d}\tau \approxeq 0.0667$ for the given time interval. We note that this time step permits detection of frequencies $\omega \lessapprox 47.1$, which is many times greater than the largest eigenfrequencies.

For each realization in the ensemble of disordered chains, we calculate the motion and the Fourier transform for the particles in the sampled region $p < M$. To obtain the ensemble frequency content, we subsequently average over the Fourier transform data for each microstate.

We emphasize that for Sects. 3.2.1 through 3.2.2, we are concerned with systems where only the masses are disordered. The coupling stiffnesses $\kappa_{(ij)} = 1$ are the same for all contacts in the chain. In Sect. 3.2.3, we vary the contact stiffnesses along with the particle masses.

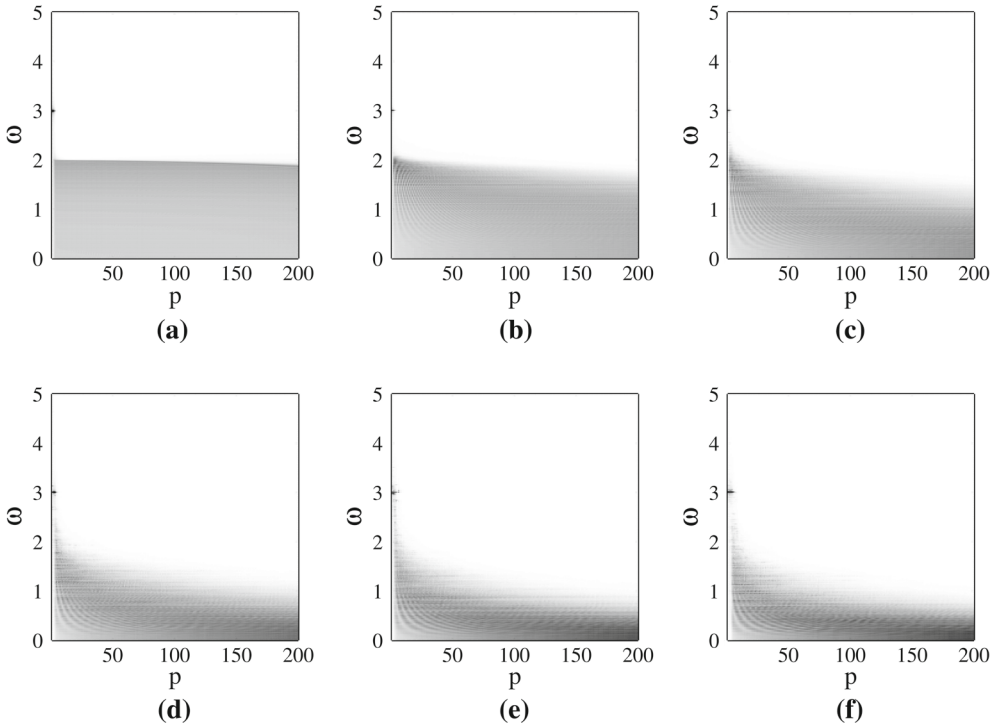

Fig. 4 Variation of the disorder parameter ξ. The source frequency $\omega_o = 3.0$ and the other parameters are the same as in Fig. 2. **a** $\xi = 0.0$, **b** $\xi = 0.1$, **c** $\xi = 0.2$, **d** $\xi = 0.35$, **e** $\xi = 0.5$, **f** $\xi = 0.55$

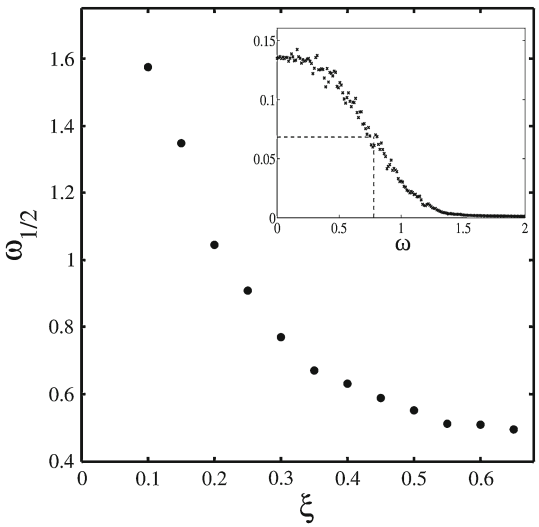

Fig. 5 Spectrum-width measure $\omega_{1/2}$ for ξ, obtained from the ensemble-averaged profiles $\langle |U^{(200)}(\omega)| \rangle$. *Inset* shows the profile of $\langle |U^{(200)}(\omega)| \rangle$ for $\xi = 0.3$

Fix ω_o, **vary** ξ: Here, we set the driving frequency $\omega_o = 3.0$ to a constant value and vary the disorder parameter ξ as shown in Fig. 4. In this manner, we may examine the effect of disorder on the transmitted frequencies. We note that the gray scale values for each subplot are the same, with the absolute Fourier component of magnitude 0.0 corresponding to white and 0.2 or greater appearing black.

From Fig. 4, we note that as the disorder parameter increases (from Fig. 4a–f) there is an associated decrease in the transmission of the relatively higher-frequency components. For ξ in the range $[0.1,\ 0.65]$, we examine the ensemble-averaged spectrum of particle $p = 200$, $\langle |U^{(200)}(\omega)| \rangle$. In accordance with the filtering behavior, the more disordered chains have a greater proportion of their content in the low frequencies. The inset of

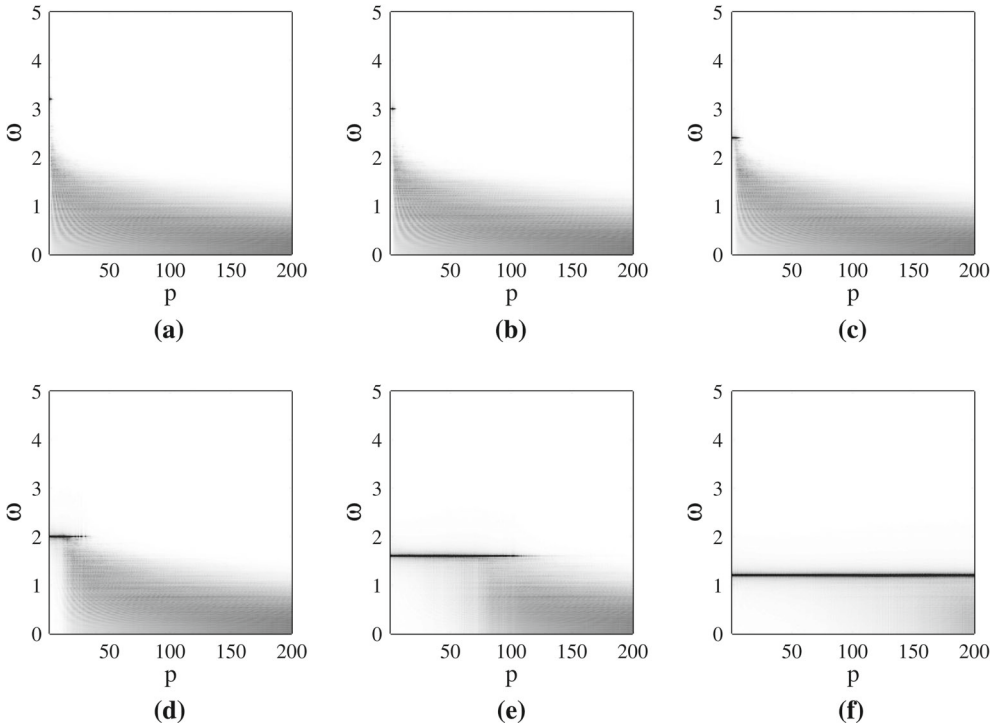

Fig. 6 Variation of the source frequency ω_o, for disorder parameter $\xi = 0.3$ and other parameters as in Fig. 2. **a** $\omega_o = 3.2$, **b** $\omega_o = 3.0$, **c** $\omega_o = 2.4$, **d** $\omega_o = 2.0$, **e** $\omega_o = 1.6$, **f** $\omega_o = 1.2$

Fig. 5 depicts $\langle |U^{(200)}(\omega)| \rangle$ for $\xi = 0.3$. Less disordered chains have a flatter profile with the decay occurring closer to $\omega = 2.0$, while more disordered chains display a higher peak and sharper decay. To quantify the effect of disorder on the spectrum width, we measure the frequency $\omega_{1/2}$ at which the curve reaches half its nominal/peak value, depicted in the inset by the dotted lines. This is performed for 10 ensembles at each ξ and plotted in Fig. 5.

As suggested by the images in Fig. 4, increasing ξ leads to an initially rapid change in the bandwidth of transmitted frequencies; as the disorder is increased further, the $(\xi, \omega_{1/2})$ curve flattens and the spectrums appear quite similar. Despite the proportionally greater number of small particles accompanying greater disorder, their presence does not appear to significantly affect the ensemble-averaged signal transmission properties (filtering) of the system. This is discussed further in Sect. 3.3.

Fix ξ, **vary** ω_o: Here, we set the disorder parameter at a constant $\xi = 0.3$ and vary the source frequency ω_o. For each driving frequency, we employ the same ensemble of 200 normally distributed random mass chains. Results for six input frequencies are shown in Fig. 6.

As suggested by the plots of Fig. 4, lower-frequency signal components are not as affected by the presence of mass disorder. This is clearly shown in Fig. 6 where the frequency components corresponding to the excitation are shown to propagate further into the system for decreasing ω_o. As evidenced by Fig. 3, low-frequency (long wavelength) oscillations of disordered arrangements capture the dispersion behavior of ordered systems and thus low-frequency inputs propagate similar to the perfect chains. This is discussed further in Sect. 3.3. Qualitatively similar results are obtained for other values of the disorder parameter ξ.

3.2.2 Frequency filtering of the linear chain: comparison of mass distributions

Here, we compare the results for different mass distributions. As detailed in Sect. 3.1, we employ normal, uniform, and binary distributions such that the first two moments are matched for a given disorder parameter ξ. In each row of Fig. 7, we plot the results for a given distribution.

Aside from small differences close to the source, we observe that the spectrum of transmitted frequencies is approximately the same for the three mass distributions studied at $\xi \leq 0.5$. The binary distribution shows more isolated frequencies penetrating the near-field, giving the figure a "rougher" appearance, but plotting the frequency spectrum $\langle |U^{(p)}(\omega)| \rangle$ for $p > 150$ (data not shown) reveals no discernible difference between the

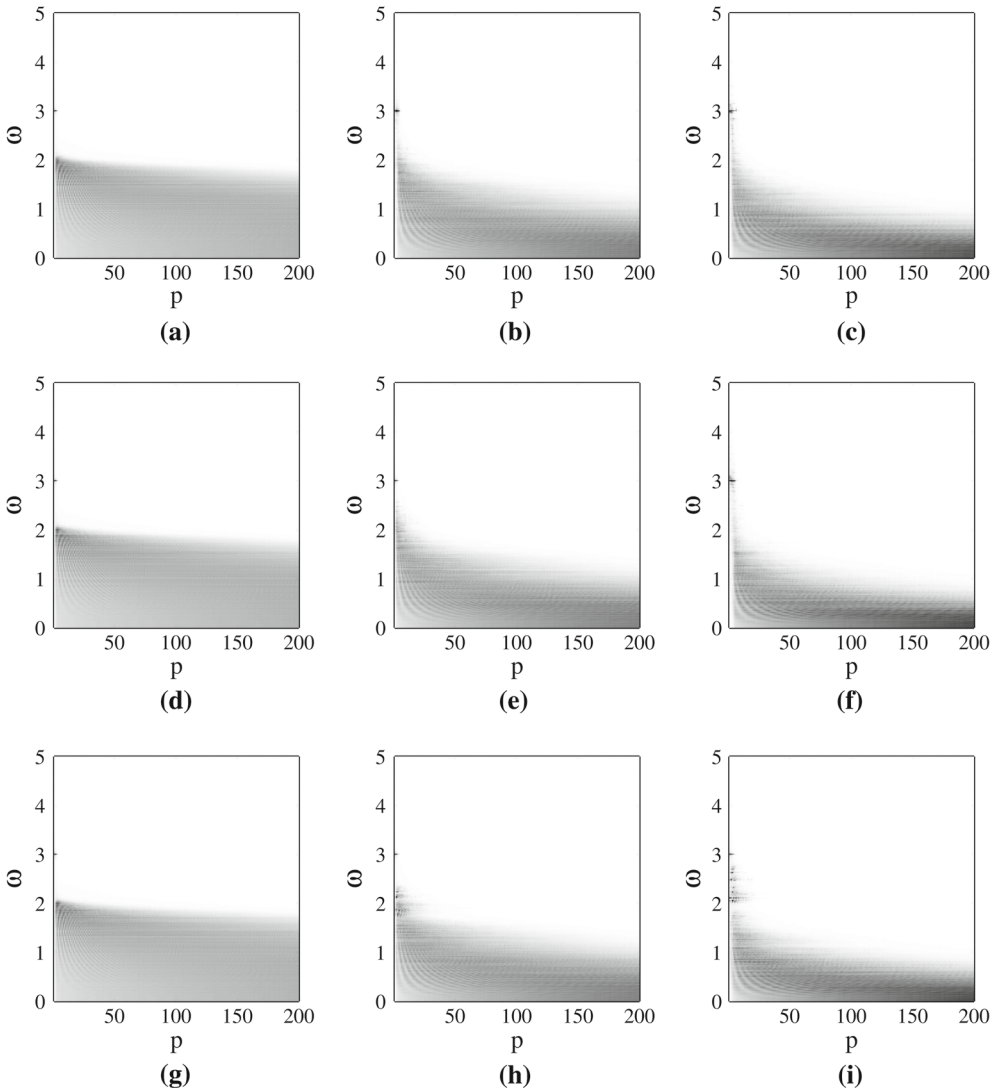

Fig. 7 Comparison of normal (**a**), (**b**), (**c**), uniform (**d**), (**e**), (**f**), and binary mass distributions (**g**), (**h**), (**i**) for $\xi = 0.1, 0.3, 0.5$, driven at $\omega_o = 3.0$.

distributions. The quantitative similarity of the transmission profiles for the binary mass system (as compared to the normal and uniformly distributed systems) suggests that the intermediate mass particles do not have a significant effect; the bulk filtering behavior is related to the interaction between the largest and smallest masses, quantified by the moments of the mass distribution. It is worth noting that higher disorder $\xi > 0.65$ does indeed result in a difference in the profiles $\langle |U^{(p)}(\omega)| \rangle$ for the binary and normal distributions. However, this is expected, as greater ξ values lead to a significant cutoff of the Gaussian tail where $b > 0$; the theoretical moments no longer correspond to the sampled distribution and comparison is no longer appropriate.

3.2.3 Frequency filtering of the mass- and contact-disordered linear chain

Here, we present results for the linearized approximation to the general nonlinear governing equations as valid for small amplitude oscillations. This is equivalent to a linear chain where the mass and contact stiffness are both disordered. The non-dimensional contact stiffness is related to the sizes of the contacting particles as given in (15). Comparison of Fig. 8a–c with the corresponding plots of Fig. 6 reveals that the addition of contact disorder leads to a more rapid spatial decay of the input frequency ω_o. We also note that the bandwidth of transmitted frequencies is marginally reduced for the contact-disordered chains, as evidenced by plotting the

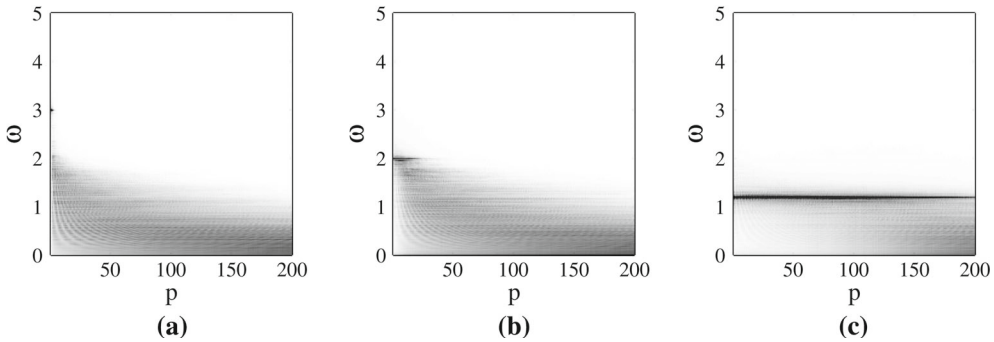

Fig. 8 Mass- and contact-disordered chain for $\xi = 0.3$ and $\omega = 3.0$ (**a**), 2.0 (**b**), 1.2 (**c**)

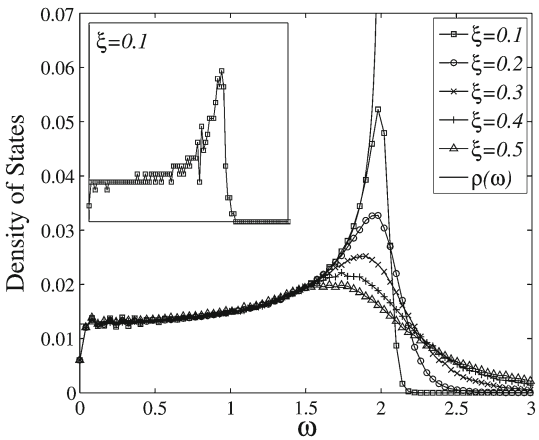

Fig. 9 Density of states for mass-disordered chains. The *curve* $\rho(\omega)$ is the analytical result (27) for the density of states in a monodisperse chain. *Inset* displays the density of states for a single chain with $\xi = 0.1$

profiles at various downstream locations (plots not shown). However, the shape of the profiles is qualitatively comparable to those of Fig. 6.

3.3 Disorder and localization

In this section, we discuss how disorder in the one-dimensional chain leads to spatial localization of the eigenmodes. Through the use of a simple fixed-end, non-driven chain, we show that this localization is responsible for the observed filtering behavior of the chains presented above. Although we mainly consider driven chains in this study, the fixed-end chain provides a convenient model system for our heuristic argument concerning high-frequency filtering.

3.3.1 Density of states

In Fig. 9, we plot the density of states for various values of the disorder parameter. The eigenvalues for 2,000 states of a 500 particle chain are numerically calculated and the density of states is normalized such that the sum of values (for each ξ) is unity, i.e., it represents the probability density function of modes as function of ω. The numerical results are plotted with the analytical result for a perfect chain as given by Sheng [45],

$$\rho(\omega) \sim \frac{1}{\sqrt{4-\omega^2}}. \tag{27}$$

In Fig. 9, the density of states increases as we approach the cutoff frequency $\omega = 2.0$ of the ordered chain. As the disorder is increased, the smaller masses permit higher-frequency oscillations and the density of states for frequencies $\omega > 2$ accordingly increases. One may observe in Figs. 2 and 4 that there is (limited) transmission of frequencies $\omega > 2.0$ for higher disorder; when $\xi = 0$, we see a very sharp cutoff at $\omega = 2.0$.

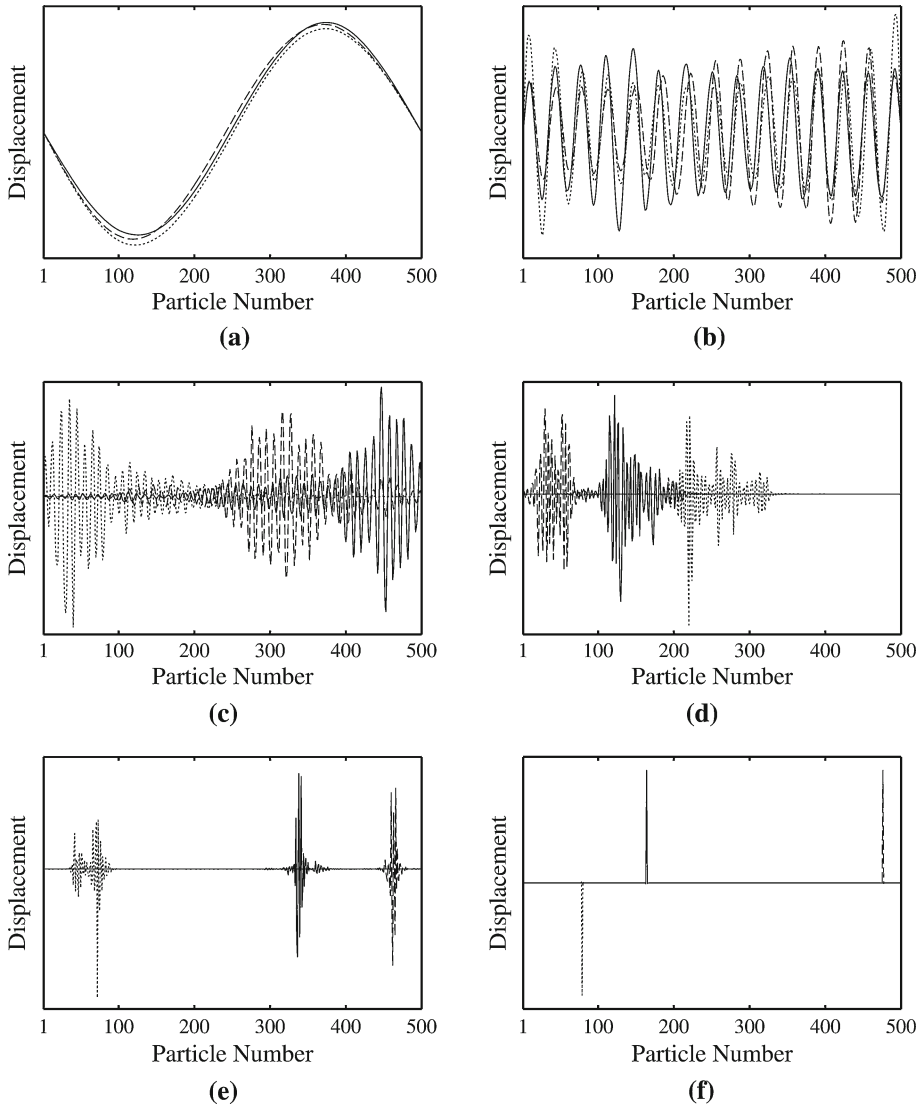

Fig. 10 Eigenmode shapes for modes $j = 2$ (**a**), 30 (**b**), 100 (**c**), 200 (**d**), 300 (**e**), 500 (**f**). Each subfigure displays the mode shape for three different random chain arrangements with disorder parameter $\xi = 0.5$

3.3.2 Localization

From Sect. 2.2, we recall the eigenvalue problem (17) for the general linear chain. In the case of monodisperse particles, the eigenvectors are sinusoids subject to the condition that the ends remain fixed. This imposes the requirement that the eigenmode wave numbers are scalar multiples of π/L, where L is the chain length between the pinned ends. For the disordered chain, we observe that eigenmodes of increasing frequency exhibit spatial mode localization. This so-called Anderson localization has been observed in many physical contexts including mechanical systems of vibrating masses [23,41].

Numerically solving the eigenvalue problem for three particular arrangements of a 500 particle random chain ($\xi = 0.5$, uniform stiffness), we plot sample eigenvectors for modes $j = 2, 30, 100, 200, 300, 500$ in Fig. 10. The low-frequency modes (e.g., Fig. 10a, b) are similarly shaped for the different chains and are "extended" in nature—the displacements are not localized about a portion of the chain as seen in the higher-frequency modes (Fig. 10c–f). In addition to the increased localization of higher-frequency modes, we note that the displacements are located at different positions in the chain, indicating sensitivity to the particular mass arrangement. The highest frequency modes approach Dirac-delta functions where only a single particle has a significant displacement (Fig. 10f). Physically, the highest frequency modes correspond to smaller mass

particles oscillating between two relatively large neighbors. We note that the large peak in the highest frequency eigenmode corresponds to the location of the smallest mass.

To investigate the effect of mode localization on the filtering behavior of random chains, we simplify the modeling by removing the driving excitation of the end-particle. With this fixed-end chain, we consider the time evolution of an initially specified waveform $\mathbf{u}_o$. The general solution derived in Sect. 2.2 reduces to

$$\mathbf{u}(x,\tau) = \mathbf{SCS}^{-1}\mathbf{u}_o, \tag{28}$$

where $\mathbf{C}$ is a diagonal matrix with $\cos\omega_{(j)}\tau$ as the (j,j) entry. Recall $\mathbf{S}$ to be the matrix of eigenvectors and $\omega_{(j)}$ as the frequency of the jth eigenmode.

3.3.3 Wave number spectra evolution with time

Just as high frequencies are observed to be filtered with distance from the driving source, high wave number/short wavelength content is observed to decay with time and only long wavelengths persist. Given the displacement history (28), we perform a spatial discrete Fourier transform (DFT) to obtain the wave number content by application of the DFT matrix [1] $\mathbf{F}$:

$$\boldsymbol{\Upsilon}(k,\tau) \equiv \mathbf{Fu}(x,\tau) = \mathbf{FSCS}^{-1}\mathbf{u}_o. \tag{29}$$

One may also differentiate Eq. (29) with respect to time (the only time dependence hidden in $\mathbf{C} = \mathbf{C}(\tau)$) to phrase this in the form of a master equation

$$\frac{d\boldsymbol{\Upsilon}}{d\tau} = \mathbf{Q}\boldsymbol{\Upsilon}, \tag{30}$$

where $\mathbf{Q}(\tau) \equiv \mathbf{FSHS}^{-1}\mathbf{F}^{-1}$, and $\mathbf{H} = \mathbf{H}(\tau) = (d\mathbf{C}/d\tau)\,\mathbf{C}^{-1}$ is a diagonal matrix with (j,j) entry $-\omega_{(j)}\tan\omega_{(j)}\tau$. The transition between wave number states is determined by the transition matrix $\mathbf{Q}$.

To examine the evolution of a particular wave component, we imagine prescribing the initial displacement to be a perfect sinusoid, subject to the fixed boundary conditions. Restricting attention to (29), we decompose this initial waveform into the sum of an eigenvector $\mathbf{s}_j$ and a difference vector $\boldsymbol{\chi}$. Thus, we write

$$\boldsymbol{\Upsilon}(k,\tau) = \mathbf{FSCS}^{-1}\left(\mathbf{s}_j + \boldsymbol{\chi}\right), \tag{31}$$

which simplifies to

$$\boldsymbol{\Upsilon}(k,\tau) = \cos\left(\omega_j\tau\right)\mathbf{Fs}_j + \mathbf{FSCS}^{-1}\boldsymbol{\chi}. \tag{32}$$

If the initially inserted waveform has a long wavelength as compared to the constituent particle sizes, see Fig. 10a, b, the decomposition suggests that $\mathbf{s}_j \approx \mathbf{u}_0$ and $\boldsymbol{\chi}$ are relatively insignificant, leaving $\boldsymbol{\Upsilon} \approx \cos\left(\omega_j\tau\right)\mathbf{Fs}_j$. The product $\mathbf{Fs}_j$, yielding the distribution of $\boldsymbol{\Upsilon}$ in k-space, would only feature contributions from a small number of long wavelengths, and the wave number content remains qualitatively similar—oscillating in time with frequency ω_j.

Conversely, if we consider inserting a small wavelength/high-frequency sinusoid $\mathbf{u}_0$, the first term of (32) is the Fourier transform of an (arbitrary) high-frequency eigenmode (e.g., Fig. 10f), which contains contributions from all wave numbers (due to its peaked, localized nature). Thus, we observe the tendency of a high-frequency mode wave to spread (distribute) its wave number content across all wave numbers. Since a strongly localized $\mathbf{s}_j$ features very few nonzero entries, one has $\boldsymbol{\chi} = \mathbf{u}_0 - \mathbf{s}_j \approx \mathbf{u}_0$, and the second term of (32) is approximately equal to $\mathbf{FSCS}^{-1}\mathbf{u}_0$, while the first is rather insignificant (alternatively one could have started directly with setting the first term to zero).

The product $\mathbf{S}^{-1}\mathbf{u}_0$ yields a vector $\mathbf{q}(\mathbf{u}_0)$ describing the linear combination of eigenvectors comprising the original waveform (for a particular chain arrangement). Writing out the terms of this matrix product, we see

$$\mathbf{FSCS}^{-1}\mathbf{u}_0 = [q_1\cos(\omega_1\tau)]\,\mathbf{Fs}_1 + \cdots + [(q_N\cos(\omega_N\tau)]\,\mathbf{Fs}_N. \tag{33}$$

Thus, the coefficients $q_1,\ldots,q_N$ determine the amplitude of oscillations for each term and $\mathbf{Fs}_j$ describes how the term's wave number content is distributed in k-space. To observe the relative magnitude of the coefficients

[1] Using e.g., the matlab function `dftmtx`.

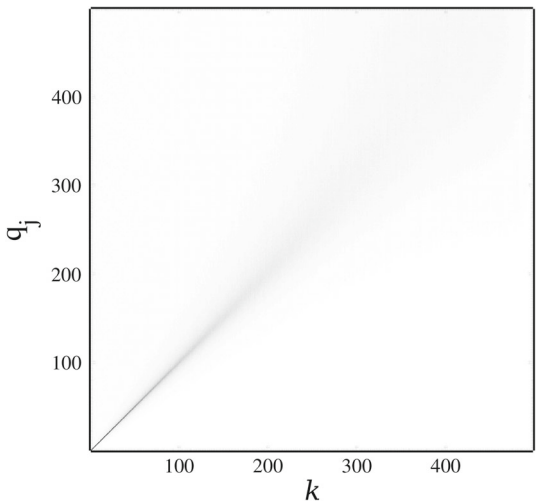

Fig. 11 Absolute values of the components of **q** (see text) for varied input waveforms $\mathbf{u}_o$, which for increasing k along the horizontal axis become wider spread out (lower *shades* of *gray*) across the eigenmodes. Results are produced for an ensemble of 200 chains of $N = 500$ particles with $\xi = 0.5$

over a range of input $\mathbf{u}_0$, we calculate $\mathbf{q}(\mathbf{u}_0)$ for 200 chains of $N = 500$ particles with $\xi = 0.5$. In Fig. 11, we plot the results in gray scale, where darker shades represent larger absolute values of the components. Increasing k along the horizontal axis corresponds to shorter wavelength initial waveforms. Vertical cross-sections (fixed k) yield the components **q** for the inserted waveform. The sharp, dark diagonal in the bottom left of the figure confirms that the coefficients corresponding to lower frequencies/longer wavelengths have greater absolute value and that long wavelengths persist. As the input wavelength is decreased, however, the relative magnitude of the coefficients is decreased and the distribution becomes spread, consistent with simulation observations in both the fixed-end and driven chains. Thus, from this simple decomposition, it is clear that mode localization is responsible for the filtering of high-frequency content in the presence of mass disorder.

3.4 Frequency filtering of the nonlinear chain

Similar to the linear chain, in Sect. 3.4.1, we perform a parameter study of ξ and ω_o for a system of normally distributed masses with Hertzian interaction. Due to the nonlinearity in the contact law, we also consider the driving amplitude ϵ. We note that the nonlinear chain is, in general, disordered in both mass and contact properties. In Sect. 3.4.2, we investigate nonlinear chains with uniform contact coupling, isolating the effect of mass disorder.

3.4.1 Frequency filtering of the nonlinear chain: normally distributed masses

Fix ω_o, **vary** ξ: Here, we set the driving frequency $\omega_o = 3.0$ and present the spectra for three values of the disorder parameter ξ in Fig. 12.

We may compare this nonlinear chain with the results of Sect. 3.2.3, where a linear contact model is employed for the mass- and contact-disordered chain. As observed in the linear system, increased disorder leads to stronger filtering of the high-frequency components. However, the profiles of transmitted frequencies are qualitatively different for the nonlinear chain. In Fig. 13, we plot the transmission profiles $\langle |U^{(200)}(\omega)| \rangle$ for a general nonlinear (with contact disorder), a contact-ordered nonlinear (see Sect. 3.4.2) and a contact-disordered linear chain (Sect. 3.2.3).

We observe that the profiles for the nonlinear chains display a sharp peak at the low frequencies, while the linear chain exhibits a flatter profile. The magnitudes of the intermediate frequency components are accordingly less in the nonlinear chain. However, we note that by changing ϵ the oscillation amplitudes will decrease such that we approach behavior that is captured by the linearized model. This is examined later, see Fig. 16.

An apparent feature of the nonlinear spectra is the "zigzag" for $\omega < 0.2$. This is not an artifact of the sampling rate or time period and the feature persists upon ensemble averaging. At a particular ξ and ω_o, the

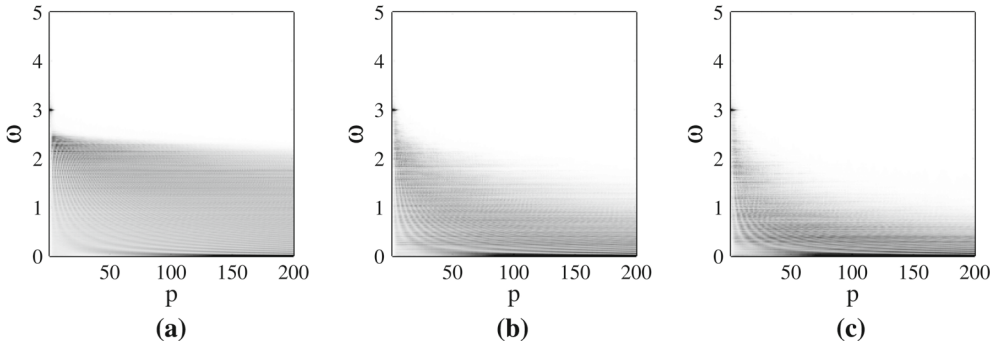

Fig. 12 Variation of disorder parameter ξ for a normal distribution of masses and Hertzian contact. Source frequency is $\omega_o = 3.0$ and the relative driving amplitude is moderate, $\epsilon = 0.05$; for a comparison of different ϵ, see Fig. 16. **a** $\xi = 0.1$, **b** $\xi = 0.3$, **c** $\xi = 0.5$

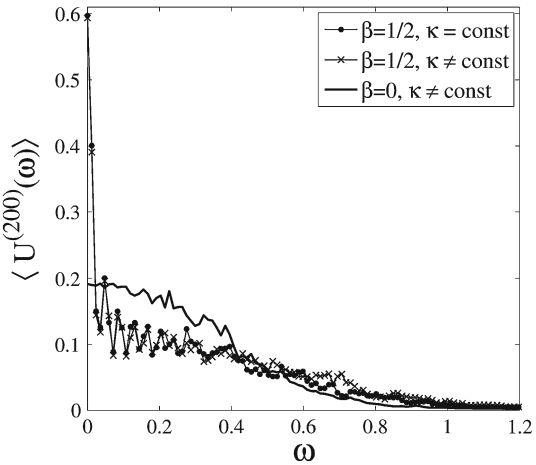

Fig. 13 Frequency spectrum at particle $p = 200$ for contact-disordered nonlinear, contact-ordered nonlinear, and contact-disordered linear chain. Parameters are $\xi = 0.5$, $\omega_o = 3.0$ and $\epsilon = 0.05$ for the nonlinear chains

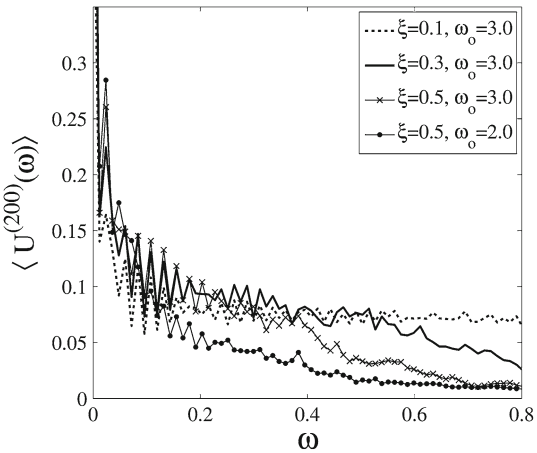

Fig. 14 Ensemble-averaged frequency spectrum at particle $p = 200$ for the nonlinear chain with $\epsilon = 0.05$. Note that changes in ξ and ω_o do not have a significant effect on the location of the "zigzag" features for low frequencies

only simulation parameter that affects the height of the peaks is the driving amplitude ϵ (see Fig. 16), which characterizes the strength of the nonlinearity through the displacements from equilibrium. In Fig. 14, we alter ξ and ω_o to show that changing the disorder (at fixed ω_o) does not have any effect on the ω location of the

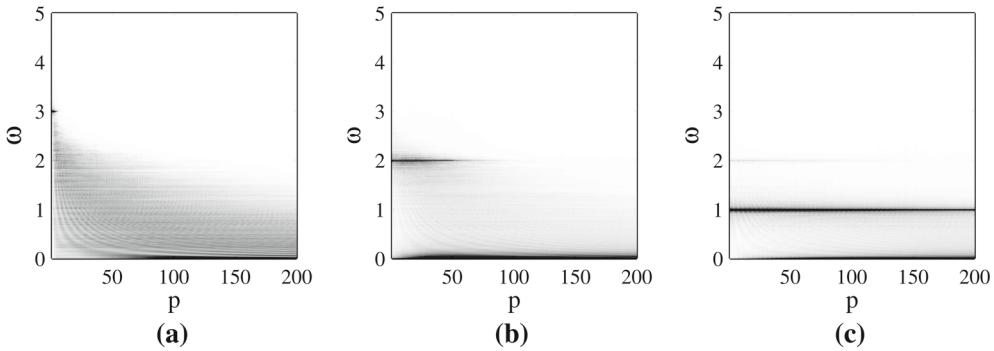

Fig. 15 Variation of source frequency ω_o. Disorder parameter is $\xi = 0.3$ and $\epsilon = 0.05$. **a** $\omega_o = 3.0$, **b** $\omega_o = 2.0$, **c** $\omega_o = 1.0$

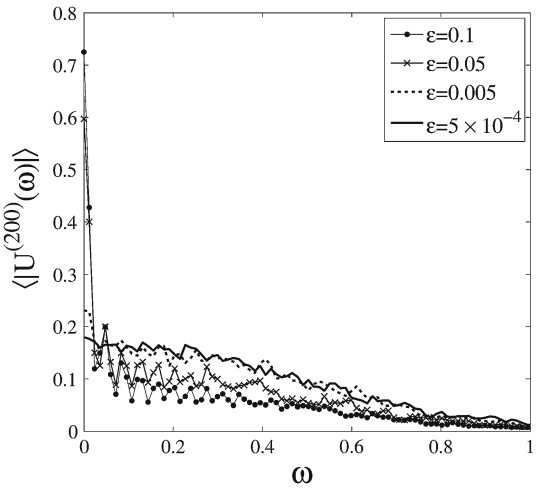

Fig. 16 Frequency spectrum at particle $p = 200$ for varied driving amplitude ϵ. Source frequency is $\omega_o = 3.0$ and $\xi = 0.5$

zigzags. Similarly, changing ω_o does not appear to have a significant effect on the locations for $\omega < 0.2$. The reason for the particular locations remains an open question.

Fix ξ, **vary** ω_o Here, we set the disorder parameter to $\xi = 0.5$ and change the driving frequency ω_o. Results are plotted in Fig. 15.

As in the linear chain, we see that lower-frequency signals are not as sensitive to the disorder of the chain, and the input frequency propagates further into the system. In Fig. 15c, we note the appearance of a harmonic at $\omega = 2\omega_o$. This frequency doubling harmonic (among others not visible due to the gray scale selection) is a general feature of nonlinear oscillations and is observed in all the simulations. Again we see that the nonlinear chain with an appropriately large excitation ($\epsilon = 0.05$ in this figure) experiences a sharp profile for $\omega \ll 1$. The penetration distance of the input frequency (e.g., for $\omega_o = 2.0$) is not affected by the driving amplitude ϵ as varying this parameter over several orders of magnitude resulted in negligible difference in the decay of this component.

Different driving amplitudes Here, the value of the non-dimensional driving amplitude ϵ is varied over several orders of magnitude: $\epsilon = 0.1, 0.05, 5 \times 10^{-3}, 5 \times 10^{-4}$. As noted with respect to Eq. (9), the non-dimensional value of ϵ measures the strength of the agitation provided by the driving with respect to the compressive external force on the chain. Thus, small values of ϵ correspond to systems with small driving and/or large confining stress. The largest driving amplitudes are set by the requirement that no contacts may open in the chain, giving $\epsilon_{\max}$ to be on the order of the characteristic overlap length scale. Simulations check this contact condition to avoid the nonlinearities associated with transient interactions.

Since the gray scale plots are qualitatively similar to prior figures (e.g., Fig. 12c) and do not resolve the fine details of the transmission profiles, we plot $\langle |U^{(200)}(\omega)| \rangle$ in Fig. 16. We note that by decreasing the driving amplitude ϵ, we decrease the magnitude of the lowest frequency components. For $\epsilon \to 0$, the profiles approach that seen in the linear chain (shown in Fig. 13), which is consistent with the linearization performed about the

equilibrium positions. The asymptotic approach to linear behavior of a compressed granular system was noted experimentally by Sinkovits et al. [46]. It is also apparent that greater ϵ causes the height of the "zigzag" peaks for $\omega < 0.3$ to grow, enforcing that this is an effect associated with the contact nonlinearity.

3.4.2 Removal of contact disorder

In a numerical realization of the monodisperse, mass-disordered setup proposed in Sect. 2.1.3, we remove the contact disorder in the Hertzian chain by setting all interaction stiffnesses to $\kappa_{(i,j)} = 1$. The frequency spectra for $p = 200$ were previously plotted in Fig. 13. Inspection of the corresponding curves reveals that contact disorder reduces the magnitude of the frequency components in the intermediate frequency range. The profiles are quite comparable for the smallest frequencies, but for $\omega > 0.4$ the spectrum for constant contact stiffness lies slightly above that of the contact-disordered case. As noted prior, similar results were obtained for the linear chains when the effects of contact disorder were considered.

4 Conclusions

In this study, we examined the frequency transmission properties of driven, disordered one-dimensional systems that behave surprisingly similar to disordered three-dimensional systems. Beginning from a general power law force–displacement relation, we investigated the behavior of pre-compressed chains, where particles interact through linear or nonlinear (Hertzian) contacts. Disordered chains behave like a low-pass frequency filter, permitting the propagation of low-frequency signals while the higher-frequency components decay with distance from the source. The signal transmission is studied as a function of the input frequency, disorder magnitude, and the choice of contact model (i.e., linear, Hertzian). As more disorder is imposed on the system, we observe that the higher relative frequencies are filtered closer to the source/driver and only low frequencies propagate in the chain. However, the results also suggest that there exists a threshold disorder after which only small changes in the ensemble-averaged properties are noted. By driving systems at various frequencies, we observe that lower-frequency signals are less sensitive to the chain arrangements and the input signal propagates further. In the context of the linear chain, we relate the filtering behavior to the localization of eigenmodes in the presence of disorder. One may imagine applications exploiting disorder effects, as could be pursued in the spirit of [5,10,13,14,32,40,47,49] where such systems were engineered to produce a desired output.

Chains composed of random, linear, contact-ordered masses sampled from different (normal, uniform, and binary) mass distributions were compared. The disorder parameter was restricted to $\xi \leq 0.5$ to ensure that only a small portion of the normal distribution ($b < 0$) was neglected. The quantitative agreement between the ensemble-averaged results between the binary and continuous distributions suggests that knowledge of the first two moments of the mass distribution is sufficient for characterizing the bulk filtering properties of these simple systems; the effect of intermediate masses is minimal.

Comparison of the nonlinear and linear systems reveals that both systems filter high frequencies in a similar manner with a decaying envelope of transmitted frequencies. However, the nonlinear chains have frequency spectra that contain much larger relative contributions from the lowest frequency components, indicated by the dramatic difference in the spectra at locations downstream from the driver. By altering the non-dimensional driving amplitude ϵ, we were able to affect the strength of the nonlinearities present; with a sufficiently small value (corresponding to small driving amplitude and/or large external compression), we recover the linear system behavior.

We examined the effect of isolated mass disorder and the combination of mass and contact disorder in both linear and nonlinear chains. Results were qualitatively similar to systems with only mass disorder; in both cases, the inclusion of contact disorder was relatively small, leading to slightly lower relative magnitudes of transmitted frequencies.

In comparing the high-frequency-filtering properties of the random one-dimensional systems to the three-dimensional packings of Mouraille and Luding [35], we note the importance of the contact geometry in their observations. Beginning from a perfect crystalline geometry, small perturbations in particle size are introduced, which created significant and dominating disorder effects in the system. The disorder (as quantified here by the distribution of particle masses) was indeed very small ($\xi \approx 0.007$) and our simulations on one-dimensional systems with disorder of this magnitude reveal no difference from perfect, monodisperse systems. This underlies the strong nonlinear effect of minimal compression and potentially transient contacts. In our consideration of compressed chains, we have avoided geometry-induced disorder. However, if the chains were

subject to very little pre-compression (approaching Nesterenko's sonic vacuum) [11,37,43], the length scale of the particle-size perturbation and the contact overlap length scale would be of the same order and strong nonlinearities could be introduced. We emphasize that we did not pursue such weakly confined systems.

Our observations about disordered one-dimensional systems may furnish clues about the role of disorder in higher-dimensional physical systems, namely the relative importance of geometry and the connection between microscale (e.g., contact length scale) properties and those at the system length scale. The investigation of this micro-macro connection and a host of nonlinear effects associated with weak pre-compression and geometrical disorder remains a rich area warranting further study. Finally, the relevance of more realistic contact mechanics (e.g. plastic deformations) [36,38] as well as the deeper understanding of idealized granular systems in higher dimensions [7,24] should help to better understand real system wave propagation in anisotropic, disordered granular matter, where wave propagation is an efficient means to measure the moduli and thus the microstructure of the material, see [19–21] and references therein.

Acknowledgments We thank S. Sterl for careful proofreading and testing of the theory. This research is supported by VICI Project No. 10828/NWO-STW.

Appendix 1: Orthogonality proof

In direct notation, for an eigenvalue/eigenvector j, the statement of the dimensionless eigenvalue problem is

$$\mathbf{A}\mathbf{s}_{(j)} = \omega_j^2 \mathbf{s}_{(j)}. \tag{34}$$

With $\mathbf{A} = -\mathbf{M}^{-1}\mathbf{K}$, we have

$$\mathbf{M}^{-1}\mathbf{K}\mathbf{s}_{(j)} = -\omega_j^2 \mathbf{s}_{(j)} \tag{35}$$

or

$$\mathbf{K}\mathbf{s}_{(j)} = -\omega_j^2 \mathbf{M}\mathbf{s}_{(j)}. \tag{36}$$

Similarly for an eigenvector k, we have

$$\mathbf{K}\mathbf{s}_{(k)} = -\omega_k^2 \mathbf{M}\mathbf{s}_{(k)}. \tag{37}$$

Taking the transpose of (37),

$$\mathbf{s}_{(k)}^{\mathrm{T}}\mathbf{K}^{\mathrm{T}} = -\omega_k^2 \mathbf{s}_{(k)}^{\mathrm{T}}\mathbf{M}^{\mathrm{T}}. \tag{38}$$

Since both $\mathbf{K}$ and $\mathbf{M}$ are symmetric, drop the transpose and then right multiply by $\mathbf{s}_{(j)}$,

$$\mathbf{s}_{(k)}^{\mathrm{T}}\mathbf{K}\mathbf{s}_{(j)} = -\omega_k^2 \mathbf{s}_{(k)}^{\mathrm{T}}\mathbf{M}\mathbf{s}_{(j)}. \tag{39}$$

Similarly, left-multiply (36) by $\mathbf{s}_{(k)}^{\mathrm{T}}$:

$$\mathbf{s}_{(k)}^{\mathrm{T}}\mathbf{K}\mathbf{s}_{(j)} = -\omega_j^2 \mathbf{s}_{(k)}^{\mathrm{T}}\mathbf{M}\mathbf{s}_{(j)}. \tag{40}$$

Subtract (40) from (39),

$$\left(\omega_j^2 - \omega_k^2\right) \mathbf{s}_{(k)}^{\mathrm{T}}\mathbf{M}\mathbf{s}_{(j)} = 0. \tag{41}$$

If $\omega_k^2 \neq \omega_j^2$, we are left with the orthogonality statement

$$\mathbf{s}_{(k)}^{\mathrm{T}}\mathbf{M}\mathbf{s}_{(j)} = 0 \quad (j \neq k) \tag{42}$$

If $j = k$, the quantity $\mathbf{s}_{(j)}^{\mathrm{T}}\mathbf{M}\mathbf{s}_{(j)} = d_{(j)} \neq 0$. Scaling each eigenvector $\mathbf{s}_{(j)}$ by $\sqrt{d_{(j)}}$, we generate an orthonormal set.

Appendix 2: Hertz contact model

With $\beta = 1/2$, we obtain the Hertz contact model and the interparticle forces are dependent on the size and material properties of the constituent particles in the following way [22]:

$$\tilde{\kappa}_{(i,j)} = \tilde{Y}_{(i,j)} \left[\frac{\tilde{r}_i \tilde{r}_j}{\tilde{r}_i + \tilde{r}_j} \right]^{1/2}, \tag{43}$$

where

$$\tilde{Y}^{-1}_{(i.j)} = \frac{3}{4} \left(\frac{1 - \nu_i^2}{\tilde{E}_i} + \frac{1 - \nu_j^2}{\tilde{E}_j} \right). \tag{44}$$

$\tilde{E}_i$ and ν_i are the elastic modulus and Poisson's ratio, respectively, of the material composing particle i. The formulation was presented for spheres but is noted to be appropriate for non-spheres as well [22]. In what follows, we choose the same material for all particles and $\tilde{Y}_{(i,j)} = \tilde{Y}$ is independent of the contact in consideration,

$$\tilde{Y}^{-1} = \frac{3}{2} \left(\frac{1 - \nu^2}{\tilde{E}} \right). \tag{45}$$

We have previously defined the characteristic length $\tilde{\ell} = \tilde{\Delta}_o$ to be the equilibrium contact overlap of two particles of the mean mass $\tilde{m}_o$. We first find the characteristic stiffness of this contact,

$$\tilde{\kappa}_o = \frac{\tilde{E}}{1 - \nu^2} \left[\frac{2\tilde{m}_o}{243\pi\tilde{\rho}} \right]^{1/6}. \tag{46}$$

With the initial overlaps defined by (3), we have

$$\tilde{\Delta}_o = \left(\frac{\tilde{P}}{\tilde{\kappa}_o} \right)^{2/3}. \tag{47}$$

The characteristic time is

$$\tilde{t}_c = \frac{1}{\tilde{\Delta}_o^{1/4}} \sqrt{\frac{1 - \nu^2}{\tilde{E}}} \left[\frac{243\pi\tilde{\rho}\tilde{m}_o^5}{2} \right]^{1/12}. \tag{48}$$

The scaled stiffness ratio at contact (i, j) simplifies to

$$\kappa_{(i,j)} = \frac{\tilde{\kappa}_{(i,j)}}{\tilde{\kappa}_o} = \sqrt{\frac{2}{b^{(i)1/3} + b^{(j)1/3}}} \left(b^{(i)} b^{(j)} \right)^{1/6}. \tag{49}$$

For a general contact, the equilibrium overlap given by (3) is

$$\tilde{\Delta}_{(i,j)} = \left(\frac{\tilde{P}}{\tilde{\kappa}_{(i,j)}} \right)^{2/3}. \tag{50}$$

Dividing by our length scale $\tilde{\Delta}_o$, the characteristic contact overlap in equilibrium is

$$\Delta_{(i,j)} = \kappa_{(i,j)}^{-2/3}. \tag{51}$$

References

1. Anderson, P.W.: Absence of diffusion in certain random lattices. Phys. Rev. **109**(5), 1492–1505 (1958)
2. Coste, C., Gilles, B.: On the validity of hertz contact law for granular material acoustics. Eur. Phys. J. B **7**, 155–168 (1999)
3. Daraio, C., Nesterenko, V.F., Herbold, E.B., Jin, S.: Energy trapping and shock disintegration in a composite granular medium. Phys. Rev. Lett. **96**, 058002 (2006)
4. Dean, P.: On disordered one-dimensional crystals. Proc. Phys. Soc. **73**, 413–421 (1959)
5. Doney, R.L., Sen, S.: Impulse absorption by tapered horizontal alignments of elastic spheres. Phys. Rev. E **72**, 041304 (2005)
6. Doney, R., Sen, S.: Decorated, tapered, and highly nonlinear granular chain. Phys. Rev. Lett. **97**(15), APS–4 (2006)
7. Donovan, J., O'Sullivan, C., Marketos, G.: Two-dimensional discrete element modelling of bender element tests on an idealised granular material. Granul. Matter **14**, 733–747 (2012)
8. Dyson, F.J.: The dynamics of a disordered linear chain. Phys. Rev. **92**(6), 1331–1338 (1953)
9. Fraternali, F., Porter, M.A., Daraio, C.: Optimal design of composite granular protectors. Mech. Adv. Mater. Struct. **17**, 1–19 (2010)
10. Gharib, M., Celik, A., Hurmuzlu, Y.: Shock absorption using linear particle chains with multiple impacts. J. Appl. Mech. **78**(3), 031005 (2011)
11. Gomez, L.R., Turner, A., Hecke, M.van , Vitelli, V.: Shocks near jamming. Phys. Rev. Lett. **108**, 058001 (2012)
12. Hall, H.E.: Solid State Physics. Wiley, London (1974)
13. Harbola, U., Rosas, A., Romero, A.H., Esposito, M., Lindenberg, K.: Pulse propagation in decorated granular chains: an analytical approach. Phys. Rev. E **80**, 051302 (2009)
14. Harbola, U., Rosas, A., Romero, A.H., Lindenberg, K.: Pulse propagation in randomly decorated chains. Phys. Rev. E **82**, 011306 (2010)
15. Herbold, E.B., Kim, J., Nesterenko, V.F., Wang, S.Y., Daraio, C.: Pulse propagation in a linear and nonlinear diatomic periodic chain: effects of acoustic frequency band-gap. Acta Mech. **205**, 85–103 (2009)
16. Jia, X., Caroli, C., Velicky, B.: Ultrasound propagation in externally stressed granular media. Phys. Rev. Lett. **82**(9), 1863–1866 (1999)
17. Job, S., Melo, F., Sokolow, A., Sen, S.: Solitary wave trains in granular chains: experiments, theory, and simulations. Granul. Matter **10**, 13–20 (2007)
18. Judge, J.A., Houston, B.H., Photiadis, D.M., Herdic, P.C.: Effects of disorder in one- and two-dimensional micromechanical resonator arrays for filtering. J. Sound Vib. **290**, 1119–1140 (2006)
19. Kumar, N., Luding, S., Magnanimo, V.: Macroscopic model with anisotropy based on micro-macro informations. Acta. Mech. doi:10.1007/s00707-014-1155-8
20. La Ragione L., Magnanimo V.: Contact anisotropy and coordination number for a granular assembly: a comparison of distinct-element-method simulations and theory. Phys. Rev. E **85**, 031304 (2012)
21. La Ragione, L., Magnanimo, V.: Evolution of the effective moduli of an anisotropic, dense, granular material. Granul. Matter. **14**(6), 749–757 (2012)
22. Landau, L., Lifschitz, E.: Theory of Elasticity. MIR, Moscow (1967)
23. Leibig, M.: Model for the propagation of sound in granular materials. Phys. Rev. E **49**(2), 1647–1656 (1994)
24. Leonard, A., Chong, C., Kevrekidis, P.G., Daraio, C.: Traveling waves in 2D hexagonal granular crystal lattices. Granul. Matter. **16** (2014). doi:10.1007/s10035-014-0487-3
25. Lieb, E.H., Mattis, D.C.: Mathematical Physics in One Dimension. Exactly soluble models of interacting particles. Academic Press, New York (1966)
26. Luding, S., Clément, E., Blumen, A., Rajchenbach, J., Duran, J.: Studies of columns of beads under external vibrations. Phys. Rev. E **49**(2), 1634 (1994)
27. Machado, L.P., Rosas, A., Lindenberg, K.: Momentum and energy propagation in tapered granular chains. Granul. Matter. **15**(6), 735–746 (2013)
28. Manciu, M., Sen, S., Hurd, A.J.: The propagation and backscattering of soliton-like pulses in a chain of quartz beads and related problems. (i). Propagation. Phys. A **274**, 588–606 (1999)
29. Manciu, M., Sen, S., Hurd, A.J.: The propagation and backscattering of soliton-like pulses in a chain of quartz beads and related problems. (ii). Backscattering. Phys. A **274**, 607–618 (1999)
30. Manciu, M., Sen, S., Hurd, A.J.: Impulse propagation in dissipative and disordered chains with power-law repulsive potentials. Phys. D **157**, 226–240 (2001)
31. Manjunath, M., Awasthi, A.P., Geubelle, P.H.: Plane wave propagation in 2D and 3D monodisperse periodic granular media. Granul. Matter. **16**, 141–150 (2014)
32. Melo, F., Job, S., Santibanez, F., Tapia, F.: Experimental evidence of shock mitigation in a hertzian tapered chain. Phys. Rev. E **73**, 041305 (2006)
33. Montroll, E.W., Potts, R.B.: Effect of defects on lattice vibrations. Phys. Rev. **100**(2), 525–543 (1955)
34. Mouraille, O.: Sound propagation in Dry Granular Materials: Discrete Element Simulations, Theory, and Experiments. Ph.D. thesis, Universiteit Twente (2009)
35. Mouraille, O., Luding, S.: Sound wave propagation in weakly disperse polydisperse granular materials. Ultrasonics **48**(6–7), 498–505 (2008)
36. Musson, R.W., Carlson, W.: Simulation of solitary waves in a monodisperse granular chain using COMSOL multiphysics: localized plastic deformation as a dissipation mechanism. Granul. Matter. (16) (2014). doi:10.1007/s10035-014-0499-z
37. Nesterenko, V.F.: Propagation of nonlinear compression pulses in granular media. J. Appl. Mech. Tech. Phys. **24**, 733–743 (1983)
38. Pal, R.K., Awasthi, A.P., Geubelle, P.H.: Wave propagation in elasto-plastic granular systems. Granul. Matter. **15**(6), 747–758 (2013)
39. Ponson, L., Boechler, N., Lai, Y.M., Porter, M.A., Kevrekidis, P.G., Daraio, C.: Nonlinear waves in disordered diatomic granular chains. Phys. Rev. E **82**, 021301 (2010)

40. Pöschel, T., Brilliantov, N.V.: Extremal collision sequences of particles on a line: optimal transmission of kinetic energy. Phys. Rev. E **63**(2), Art no:021505 (2000)
41. Rosenstock, H.B., McGill, R.E.: Vibrational modes of disordered linear chains. J. Math. Phys. **3**(1), 200–202 (1962)
42. Schmidt, H.: Disordered one-dimensional crystals. Phys. Rev. **105**(2), 425–441 (1957)
43. Sen, S., Hong, J., Bang, J., Avalos, E., Doney, R.: Solitary waves in the granular chain. Phys. Rep. **462**, 21–66 (2008)
44. Sen, S., Manciu, M., Wright, J.D.: Solitonlike pulses in perturbed and driven hertzian chains and their possible applications in detecting buried impurities. Phys. Rev. E **57**(2), 2386–2397 (1998)
45. Sheng, P.: Introduction to Wave Scattering, Localization and Mesoscopic Phenomena. Springer, Berlin (2006)
46. Sinkovits, R.S., Sen, S.: Nonlinear Dynamics in Granular Columns. Phys. Rev. Lett. **74**(14), 2686 (1995)
47. Sokolow, A., Pfannes, J.M., Doney, R.L., Nakagawa, M., Agui, J.H., Sen, S.: Absorption of short duration pulses by small, scalable, tapered granular chains. Appl. Phys. Lett. **87**, 254104 (2005)
48. Tournat, V., Gusev, V.E., Castagnède, B.: Self-demodulation of elastic waves in a one-dimensional granular chain. Phys. Rev. E **70**(2), 056603 (2004)
49. Wu, D.T.: Conservation principles in solitary impulse propagation through granular chains. Phys. A **315**, 194–202 (2002)
50. Ziman, J.M.: Principles of the Theory of Solids, 2nd edn. Cambridge University Press, Cambridge (1972)